Available online at www.sciencedirect.com
ScienceDirect
Journal of Solid State Chemistry 180 (2007) 1083–1092
JOURNAL OF SOLID STATE CHEMISTRY
www.elsevier.com/locate/jssc

# Structures and phase diagram for the system $CaTiO_3$–$La_{2/3}TiO_3$

Zhaoming Zhang[a,*], Gregory R. Lumpkin[a,b], Christopher J. Howard[a], Kevin S. Knight[c], Karl R. Whittle[b,d], Keiichi Osaka[e]

[a]*Australian Nuclear Science and Technology Organisation, Private Mail Bag 1, Menai, NSW 2234, Australia*
[b]*Department of Earth Sciences, University of Cambridge, Downing Street, Cambridge CB2 3EQ, UK*
[c]*ISIS Facility, Rutherford Appleton Laboratory, Chilton, Didcot OX11 0QX, UK*
[d]*Department of Engineering Materials, University of Sheffield, Sir Robert Hadfield Building, Mappin Street, Sheffield S1 3JD, UK*
[e]*Japan Synchrotron Radiation Research Institute/SPring-8, 1-1-1 Kouto, Sayo-cho, Sayo-gun, Hyogo 679-5198, Japan*

Received 24 August 2006; received in revised form 21 December 2006; accepted 4 January 2007
Available online 14 January 2007

**Abstract**

High-resolution neutron and synchrotron X-ray powder diffraction have been used to examine various compositions across the system $(1-x)CaTiO_3-xLa_{2/3}TiO_3$. The structures at room temperature were determined according to composition: in *Pbnm* for $0 \leqslant x \leqslant 0.5$, *Ibmm* for $0.5 < x < 0.7$, then *I*4/*mcm* for $0.7 \lesssim x < 0.9$, and finally in *Cmmm* for $x \geqslant 0.9$. Although the four structures are the same as those proposed previously in an X-ray diffraction study, the phase boundaries are somewhat different, in particular the *Pbnm* ↔ *Ibmm* phase boundary has been extended from $x \lesssim 0.4$ to $x > 0.5$ in the current study based on our high-resolution neutron diffraction data. From *in situ* measurements to identify structures above room temperature, an approximate composition–temperature phase diagram has been constructed, involving four temperature-induced phase transitions: *Pbnm* → *I*4/*mcm*, *Ibmm* → *I*4/*mcm*, *I*4/*mcm* → $Pm\bar{3}m$ and *Cmmm* → *P*4/*mmm*.


*Keywords:* Perovskites; Crystal structures; Octahedral tilting; Cation/vacancy ordering; Phase diagram; Neutron powder diffraction; Synchrotron X-ray diffraction

## 1. Introduction

Cation-deficient perovskites show high ionic conductivity indicating a considerable potential for use in solid oxide fuel cells [1,2], and these materials exhibit unique dielectric properties as well [3]. In spite of this, the crystal structures of cation-deficient perovskites such as $La_{2/3}TiO_3$ and $Nd_{2/3}TiO_3$ have until very recently been poorly understood [4]. In consequence, pseudo-binary systems such as $SrTiO_3$–$La_{2/3}TiO_3$ and $CaTiO_3$–$La_{2/3}TiO_3$ also have been incompletely understood. The present study follows elucidation of the crystal structure of $La_{2/3}TiO_3$, as stabilised by assorted dopants [5–7], and our own successful study of the system $SrTiO_3$–$La_{2/3}TiO_3$ [8].

The crystal structures in these cation-deficient perovskites are determined by the disposition of vacancies across the perovskite *A*-sites, and the tilting of the $TiO_6$ octahedra. At low La concentrations, hence low concentrations of vacancies (there is one vacancy for every two La atoms in this system), the vacancies are thought to be distributed at random, except perhaps for some association of vacancies with $La^{3+}$ ions. At high La/vacancy concentrations, there is an energy advantage in the accumulation of vacancies into alternate planes when accompanied by the movement of the *B*-site (Ti) cations toward and the anions away from these underpopulated *A*-site planes [9]. There is ample experimental evidence, from diffraction studies ([6] and references therein), that in the La-rich compounds vacancies do indeed accumulate onto alternate *A*-site planes, that is there is a layered ordering involving the alternation of cation-rich and cation-poor planes. At intermediate La concentrations, a degree of layered ordering might be expected as in the $SrTiO_3$–$La_{2/3}TiO_3$ system [8]. Octahedral tilting in perovskites has long been the subject of intensive study ([10] and references

*Corresponding author. Fax: +61 2 9543 7179.
*E-mail address:* zhaoming.zhang@ansto.gov.au (Z. Zhang).

0022-4596/$ - see front matter © 2007 Elsevier Inc. All rights reserved.
doi:10.1016/j.jssc.2007.01.005

therein), and the different possible tilt systems are described in terms of the component tilts around the *x*-, *y*- and *z*-axes of the parent perovskite, making use of Glazer's notation [11,12]. Because of the corner connections of the $BO_6$ octahedra the tilting of one octahedron around any of these axes completely determines the tilting in the plane perpendicular to that axis. The tilting of octahedra in the next plane along the axis must be the same in magnitude but can be either in the same (in-phase) or opposite (out-of-phase) sense. Glazer's symbol then is of the form $a^{\#}b^{\#}c^{\#}$ in which the literals refer in turn to tilts around the parent *x*-, *y*- and *z*-axes and the superscript # takes the values +, −, 0 to indicate in-phase, out-of-phase, and no tilting, respectively. The repetition of a letter indicates both tilt angles and lattice repeats, relating to the corresponding axes, are equal. The crystal structures corresponding to the different tilt systems with or without layered cation/vacancy ordering have been obtained using group theory and recorded elsewhere [10,13]. The experimental determination of the crystal structures thus reduces to the search for evidence for layered cation/vacancy ordering and the nature of the tilts involved.

The room temperature structure of the $CaTiO_3$ end member was established long ago [14]. It is orthorhombic in space group *Pbnm*, tilt system $a^-a^-c^+$. At 1498 K it undergoes a discontinuous transition to a tetragonal structure, space group *I*4/*mcm*, tilt system $a^0a^0c^-$, then at 1634 K a continuous transition to the basic cubic structure, space group $Pm\bar{3}m$, tilt system $a^0a^0a^0$ ([15] and references therein). As mentioned at the outset, the room temperature structure for the other end member $La_{2/3}TiO_3$ has been elucidated only very recently [5–7]. It is orthorhombic, in space group *Cmmm*, and the tilt system is $a^-b^0c^0$. Upon heating, there is a continuous transition as the tilt vanishes (but the layered ordering remains), and the structure at elevated temperature is tetragonal, space group *P*4/*mmm*, tilt system $a^0a^0c^0$. The temperature of the orthorhombic to tetragonal transition has been reported as 633 K in $La_{0.6}Sr_{0.1}TiO_3$ [6], 623 K in $La_{0.68}Ti_{0.95}Al_{0.05}O_3$ [16], 643 K in $La_{0.63}Ti_{0.92}Nb_{0.08}O_3$ [17], and 784 K in $La_{0.6}Ca_{0.1}TiO_3$ [18]. Vashook and co-workers [19,20] have carried out mostly room temperature studies across the $(1-x)CaTiO_3$–$xLa_{2/3}TiO_3$ system using X-ray diffraction, and reported four structures according to composition: in *Pbnm* (as for $CaTiO_3$) for $0 \leqslant x < 0.4$, then *Ibmm* for $0.4 \leqslant x < 0.7$, *I*4/*mcm* for $0.7 \leqslant x < 0.8$, and finally in *Cmmm* for $0.8 \leqslant x \leqslant 0.96$ (as for the end member $La_{2/3}TiO_3$). However, this system covers a wide range of compositions in pseudo-cubic symmetry ($0.4 \leqslant x \leqslant 0.8$), which means that the correct structural identification relies on the presence of superlattice reflections (arising from octahedral tilting in this case). Since octahedral tilting involves the movement of oxygen ions only, the corresponding superlattice reflections would show more strongly in neutron diffraction patterns than X-ray ones. Therefore, we considered it worthwhile to revisit this system using neutron diffraction measurements. Based on our high-resolution neutron diffraction data, we were able to prove that the correct space group for the orthorhombic structure at $x = 0.4$ and 0.5 is *Pbnm*, not *Ibmm* as previously reported. Vashook and co-workers also carried out high-temperature studies on a small number of compositions ($x = 0.4$, 0.9, 0.96) [18,19]. We have conducted studies on additional compositions using both neutron and synchrotron X-ray diffraction searching for phase transitions, so that a temperature–composition phase diagram could be constructed.

## 2. Experimental

Samples of $Ca_{(1-x)}La_{2x/3}TiO_3$ at $x = 0.1$, 0.2, 0.3, 0.4, 0.5, 0.6, 0.7, 0.8 and 0.9 were produced by the standard ceramic solid state technique. Stoichiometric quantities of $CaCO_3$ (Alfa-Aesar, 99.9%), $La_2O_3$ (Aldrich, 99.5%) and $TiO_2$ (Alfa-Aesar, 99.9%) powders were mixed and ground with ethanol in a ball mill. After drying, the mixtures were heated in air at 1373 K for 1 day and then at 1523 K for 2 days, with cooling and regrinding after the initial heating step. The crystallinity and phase purity of the products were checked using laboratory powder X-ray diffraction with Cu $K_\alpha$ radiation. The $x = 0$ end member, $CaTiO_3$, was a high-purity powder sample purchased from Aldrich.

Time-of-flight powder neutron diffraction data were recorded at room temperature for all samples using the high-resolution powder diffractometer, HRPD, at the ISIS neutron facility, Rutherford Appleton Laboratories, UK [21]. The ground samples were loaded into thin-walled 11 mm diameter vanadium sample cans, which were then suspended from the standard ISIS candlesticks. Diffraction patterns from the samples were recorded over the time-of-flight range 30–130 ms in both back-scattering and 90° detector banks, corresponding to *d*-spacings from 0.6 to 2.6 Å (at a resolution $\Delta d/d \sim 4 \times 10^{-4}$) and from 0.9 to 3.7 Å ($\Delta d/d \sim 2 \times 10^{-3}$), respectively. The patterns were normalised to the incident beam spectrum as recorded in the upstream monitor, and corrected for detector efficiency according to prior calibration with a vanadium scan. Patterns were recorded to a minimum total incident proton beam of about 75 μA h at room temperature, corresponding to ~2.3 h of data collection, to allow good structure determinations. High-temperature neutron diffraction patterns were also obtained for $Ca_{0.7}La_{0.2}TiO_3$ ($x = 0.3$) up to 1173 K, with the vanadium sample can mounted in an ISIS designed furnace. The RAL furnace employs a cylindrical vanadium element and operates under high vacuum (pressure $< 10^{-4}$ mbar). The thermometry is based on type-K (chromel–alumel) thermocouples, the controlling one positioned in contact with the sample can at about 20 mm above the beam centre. The sample temperature was controlled to ±0.5 K. The high-temperature patterns were first collected in 100 K steps from 373 to 1173 K to a total incident proton beam of about 75 μA h, then in 10 K steps down to 1073 K to a total incident proton beam of about 35 μA h (finer temperature intervals but shorter counting time in order to follow the phase transition in detail). In

order to allow for thermal equilibration of the sample, data collection was delayed for a period of at least 5 min (depending on the size of the temperature step) after the stability at the set point had been achieved.

High-temperature studies for other samples, $Ca_{(1-x)}La_{2x/3}TiO_3$ with $x = 0.4$, 0.5, 0.8 and 0.9, were carried out using the high-resolution X-ray powder diffractometer installed on beam line BL02B2, at the SPring-8 synchrotron, Hyogo, Japan [22]. The wavelength was 0.7765 Å as determined by calibration with a $CeO_2$ standard specimen. The finely ground samples were housed in 0.2 mm quartz capillaries. All the diffraction patterns were recorded to 75° (2$\theta$) on a single image plate. High temperatures were achieved using a heated nitrogen gas flow, and measured using a type-K thermocouple located at the head of the nozzle. Patterns were recorded at (sample) temperatures from 300 up to 980 K. The temperature intervals were typically 50 K, but varied from 25 to 100 K depending on the perceived proximity to phase transitions. For $Ca_{0.3}La_{0.47}TiO_3$ ($x = 0.7$), diffraction patterns were obtained from 100 to 350 K with a temperature interval of 50 K. Experimental details for the low-temperature measurements are the same as those described above, except that a glass capillary was used to house the powder sample and the heated nitrogen gas flow was replaced by a cooled one.

The neutron diffraction patterns were fitted using the Rietveld method [23] as implemented in the GSAS computer program [24,25]. Patterns from both the back-scattering and the 90° detector banks were fitted simultaneously, the diffractometer constant for the 90° bank being released to ensure that the lattice parameters were determined by the higher-resolution back-scattering bank in every case. The peak shapes were modelled as convolutions of exponentials with a pseudo-Voigt in which two peak width parameters were varied, and the background as Chebyshev polynomials [24]. Displacement parameters were refined along with internal co-ordinates, and oxygen displacement parameters were taken to be anisotropic. The isotropic displacement parameters for the two *A*-site cations, $Ca^{2+}$ and $La^{3+}$, were constrained to be equal. For $Ca_{0.1}La_{0.6}TiO_3$ ($x = 0.9$), the distribution of the $La^{3+}$/$Ca^{2+}$ ions over the two crystallographically distinct *A*-sites was allowed to vary, with the sum of the La and Ca occupancies of these two sites constrained to 1.2 and 0.2, respectively. Certain peaks seen to be broadened (*M*- or *R*-point peaks—see next section) were distinguished using the 'stacking fault' model within the GSAS computer program [24], then fitted with larger peak widths than the rest of the peaks.

## 3. Results and discussion

### 3.1. Room temperature studies

Extracts from the neutron diffraction patterns, $1.6 < d < 2.5$ Å, recorded from $Ca_{(1-x)}La_{2x/3}TiO_3$ ($x = 0$–0.9) at room temperature are shown in Fig. 1. The peaks in the figure are identified by indices based on the $1 \times 1 \times 1$ parent perovskite subcell. Peaks with all integral indices correspond to peaks from the ideal cubic aristotype. The superlattice peaks are also indexed on the basis of the $1 \times 1 \times 1$ cell, and marked as *R*-point (all half-integral indices), *M*-point (one integral, two half-integral indices), and *X*-point (two integral, one half-integral indices). Intensities at the *R*- and *M*-points arise from out-of-phase (−) and in-phase (+) octahedral tilting, respectively, and those at the *X*-point show contributions either from the *M*- and *R*-point distortions acting in concert [26], or from *A*-site cation/vacancy ordering. An important first step in any data analysis is the inspection of diffraction patterns, with a view to identifying the structures obtained. The main perovskite peaks were inspected for broadening or splitting, which would indicate a tetragonal or orthorhombic distortion accompanying cation ordering and/or octahedral tilting. In addition, a search was made for superlattice peaks, at the *R*-, *M*- and *X*-points.

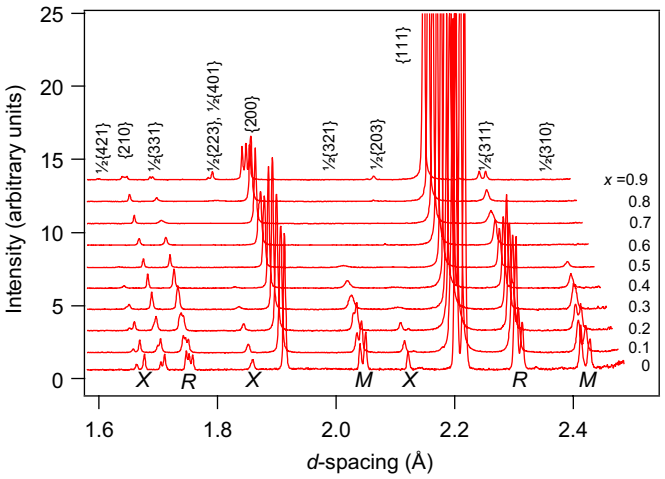


Fig. 1. Extracts ($1.6 < d < 2.5$ Å) from the neutron diffraction patterns, as recorded in the back-scattering detector bank, from samples of $Ca_{(1-x)}La_{2x/3}TiO_3$ at room temperature. The groups of peaks are indexed on the basic perovskite subcell—the brackets here are intended to refer to a set of reflections that would be equivalent for the cubic perovskite. Superlattice peaks at the *M*- and *R*-points arise from in-phase (+) and out-of-phase (−) tilting of the $TiO_6$ octahedra, respectively, while superlattice peaks at the *X*-points arise either from the combined action of in-phase and out-of-phase tilting, or cation/vacancy ordering on the perovskite *A*-sites, depending on composition.

Using the protocol described above, we identified the structures as being orthorhombic in space group *Pbnm*, as for the $CaTiO_3$ end member, for $Ca_{(1-x)}La_{2x/3}TiO_3$ at $x = 0.1$, 0.2, 0.3, 0.4 and 0.5. The tilt system is described in Glazer's notation as $a^-a^-c^+$; the presence of both in-phase and out-of-phase tilting was indicated clearly by the intensities at both *M*- and *R*-points in the diffraction patterns. Weaker intensities were also observed at the *X*-point, due to the combined action of in-phase and out-of-phase tilting (*not* cation/vacancy ordering). Our results

differ from previous X-ray work [19,20], in which *Ibmm* (tilt system $a^-a^-c^0$) was assigned as the space group for $Ca_{(1-x)}La_{2x/3}TiO_3$ at $x = 0.4$ and 0.5 (or $Ca_xLa_{2(1-x)/3}TiO_3$ at $x = 0.6$ and 0.5), presumably because the *M*-point reflections at these compositions were too weak to be visible in the X-ray patterns. In contrast, the intensities at *M*-points in our neutron patterns for $Ca_{(1-x)}La_{2x/3}TiO_3$ at $x = 0.4$ and 0.5 were unmistakable, as illustrated in Fig. 2(a). This confirms that neutron diffraction is particularly valuable for monitoring octahedral tilting. In addition, our high-resolution neutron diffraction data revealed systematic broadening of the *M*- (and consequently *X*-) point superlattice reflections for $Ca_{(1-x)}La_{2x/3}TiO_3$ at $x = 0.2$–0.5, the degree of broadening increasing with $x$. Recalling that the *M*- point superlattice reflections arise from in-phase tilting of the $TiO_6$ octahedra, we attribute this broadening to the occasional reversal of the sense of this tilting, which could occur within an otherwise unaltered framework and so not impact on the other peaks. In other words, we believe this to be kind of a (domain) size broadening, reflecting that the coherence of the in-phase octahedral tilting is maintained over only a rather limited range.

For $Ca_{0.4}La_{0.4}TiO_3$ ($x = 0.6$), there was no longer intensity at the *M*-point (Fig. 2(a)), this indicating a different structure, without any in-phase octahedral tilting. As there are no other qualitative changes in the diffraction patterns, the structure should be either orthorhombic in *Ibmm* ($a^-a^-c^0$) or tetragonal in *I*4/*mcm* ($a^0a^0c^-$). Based on Glazer's rigid octahedron model [11,12], the expected relationships among the parent cell parameters are $a_p < b_p = c_p$ and $a_p = b_p < c_p$ for *Ibmm* and *I*4/*mcm* structures, respectively. Upon close inspection of the doublet at $d \sim 1.93$ Å ($x = 0.6$ in Fig. 2(b)), indexed as $\{200\}_p$ on the parent subcell, it is clear that this peak has higher intensity on the high-$d$ side (i.e., $a_p < b_p = c_p$). Therefore, we agree with the previously proposed structure in *Ibmm* [19,20]. The similarity of diffraction patterns across the boundary from *Pbnm* (apart from the vanishing of the *M*-point reflections) also suggests that the transition from that structure might be continuous, in which case the structure in *Ibmm* would be the only possibility [10].

When $x$ is increased from 0.6 to 0.7, the most visible changes in the diffraction pattens are the decreased intensities at the *R*-point reflections. However, the more significant change occurs with the above mentioned doublet $\{200\}_p$, which has collapsed into a singlet (Fig. 2(b)). This means that the structure is pseudo-cubic for $Ca_{0.3}La_{0.47}TiO_3$ ($x = 0.7$), and both *Ibmm* and *I*4/*mcm* are now possible space groups. In other words, this structure cannot be determined unambiguously based on room temperature powder diffraction data alone. We carried out refinements assuming both structural models, and the goodness-of-fit is practically the same. However, the peak position of the *R*-point reflection at $d \sim 2.33$ Å seems to be better described using the structural model in *I*4/*mcm*. Therefore, we tentatively consider the room temperature structure for $Ca_{0.3}La_{0.47}TiO_3$ ($x = 0.7$) as tetragonal in *I*4/*mcm* and the phase boundary between *Ibmm* and *I*4/*mcm* at just below this composition ($x \lesssim 0.7$). As shown in the next section, this assignment is consistent with the phase diagram derived from high-temperature measurements. It is worthwhile noting that another subtle difference in the diffraction patterns between $x = 0.6$ and

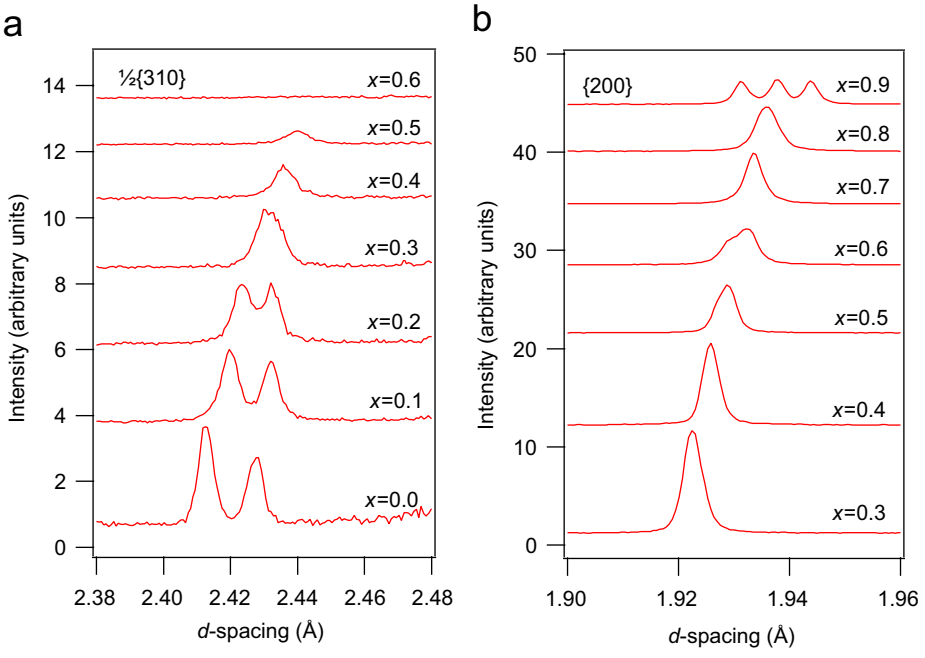


Fig. 2. Extracts from the neutron diffraction patterns—as recorded in the back-scattering detector bank: (a) $2.38 < d < 2.48$ Å, and (b) $1.90 < d < 1.96$ Å, showing the evolution of the $\frac{1}{2}\{310\}_p$ (*M*-point) and $\{200\}_p$ reflections (indexed on the basic perovskite subcell) as a function of composition.

0.7 is the broadened *R*-point peaks for $x = 0.7$, suggesting short-range order associated with the out-of-phase octahedral tilting. Although no *X*-point reflections were observed in the neutron diffraction patterns, they appeared as very weak and broad features in the synchrotron X-ray patterns at 300 K, indicating the onset of cation/vacancy ordering at $x \approx 0.7$. This also confirms that synchrotron powder XRD is more sensitive to cation/vacancy ordering than neutrons.

The neutron diffraction pattern for $Ca_{0.2}La_{0.53}TiO_3$ ($x = 0.8$) at room temperature is consistent with this sample having a tetragonal structure in space group *I*4/*mcm*, although the main perovskite peak still appeared to be a single symmetric peak (Fig. 2(b)). This assignment is also supported by the phase diagram obtained from high-temperature measurements (see Fig. 7). Although we could just make out the *X*-point reflections in the neutron diffraction patterns (indicating the cation/vacancy ordering has increased slightly with increasing La content—both in degree and range), these peaks are still very weak and broad and therefore not included in the refinements. In contrast, Vashook and co-workers [20] reported that the room temperature structure for $Ca_{0.2}La_{0.53}TiO_3$ ($x = 0.8$) is orthorhombic in *Cmmm*, presumably including the weak and broad *X*-point reflections in their structural refinements.

The pattern for $Ca_{0.1}La_{0.6}TiO_3$ ($x = 0.9$) is very similar to that shown in our previous report for $Sr_{0.1}La_{0.6}TiO_3$ [6]. The structure was determined as orthorhombic in space group *Cmmm* (tilt system $a^-b^0c^0$), based on the splitting of the main perovskite peaks [e.g., the $\{200\}_p$ peak is now a triplet as shown in Fig. 2(b)] and the presence of superlattice peaks at the *X*- and *R*-points (and very weak intensities at the *M*-point due to the combination of *X*- and *R*-point distortions). Pertinent features of this structure are the alternation of (almost) fully and partly occupied layers of La(Ca) cation, and out-of-phase tilting of the $TiO_6$ octahedra around an axis perpendicular to the direction of the cation ordering.

The neutron diffraction patterns were fitted using the space groups identified above, and both lattice parameters and atomic co-ordinates were determined using the Rietveld method [23–25] as outlined in the previous section. Details of the four distinct structures (represented by four compositions at $x = 0.3$, 0.6, 0.8 and 0.9), are included in Table 1.

Fig. 3(a) shows suitably scaled cell parameters as a function of composition ($x$) at room temperature (data for $x = 0.7$ were obtained assuming the tetragonal structure in *I*4/*mcm*). The following phase boundaries are presented by dashed vertical lines to indicate the change of space groups:

Table 1
Lattice parameters, Wyckoff sites, atomic fractional coordinates, occupancies, and displacement parameters of the room temperature structures for $Ca_{0.7}La_{0.2}TiO_3$, $Ca_{0.4}La_{0.4}TiO_3$, $Ca_{0.2}La_{0.53}TiO_3$ and $Ca_{0.1}La_{0.6}TiO_3$

| Atom | Site | *x* | *y* | *z* | Occupancy | $U$ ($10^{-2}$ Å$^2$) |
|---|---|---|---|---|---|---|
| $Ca_{0.7}La_{0.2}TiO_3$ | | | | | | |
| *Pbnm*, $a = 5.4285(1)$, $b = 5.4464(1)$, $c = 7.6851(1)$ Å, $R_{wp} = 4.92\%$, $R_p = 4.65\%$ | | | | | | |
| Ca/La | 4*c* | 0.0065(4) | 0.5242(2) | 0.25 | 0.7/0.2 | 1.35(2) |
| Ti | 4*a* | 0 | 0 | 0 | 1 | 0.96(3) |
| O1 | 4*c* | −0.0623(3) | −0.0104(3) | 0.25 | 1 | 1.39(9) |
| O2 | 8*d* | 0.2158(2) | 0.2809(2) | 0.0311(2) | 1 | 1.48(5) |
| $Ca_{0.4}La_{0.4}TiO_3$ | | | | | | |
| *Ibmm*, $a = 5.4651(2)$, $b = 5.4637(1)$, $c = 7.7125(1)$ Å, $R_{wp} = 6.32\%$, $R_p = 5.12\%$ | | | | | | |
| Ca/La | 4*e* | −0.0074(10) | 0.5 | 0.25 | 0.4/0.4 | 1.43(3) |
| Ti | 4*a* | 0 | 0 | 0 | 1 | 1.00(3) |
| O1 | 4*e* | −0.0454(5) | 0 | 0.25 | 1 | 2.08(16) |
| O2 | 8*g* | 0.25 | 0.25 | 0.0258(2) | 1 | 2.75(20) |
| $Ca_{0.2}La_{0.53}TiO_3$ | | | | | | |
| *I*4/*mcm*, $a = b = 5.4709(1)$, $c = 7.7475(1)$ Å, $R_{wp} = 7.28\%$, $R_p = 5.68\%$ | | | | | | |
| Ca/La | 4*b* | 0 | 0.5 | 0.25 | 0.2/0.53 | 1.36(3) |
| Ti | 4*c* | 0 | 0 | 0 | 1 | 1.32(4) |
| O1 | 4*a* | 0 | 0 | 0.25 | 1 | 3.10(16) |
| O2 | 8*h* | 0.2227(2) | 0.2773(2) | 0 | 1 | 1.90(7) |
| $Ca_{0.1}La_{0.6}TiO_3$ | | | | | | |
| *Cmmm*, $a = 7.7489(1)$, $b = 7.7228(1)$, $c = 7.7733(1)$ Å, $R_{wp} = 4.81\%$, $R_p = 4.08\%$ | | | | | | |
| Ca/La 1 | 4*g* | 0.2526(4) | 0 | 0 | 0.001 /0.928(3) | 0.92(4) |
| Ca/La 2 | 4*h* | 0.2578(9) | 0 | 0.5 | 0.199 /0.272(3) | 1.16(11) |
| Ti | 8*n* | 0 | 0.2451(6) | 0.2611(2) | 1 | 0.76(3) |
| O1 | 4*i* | 0 | 0.2754(4) | 0 | 1 | 1.24(15) |
| O2 | 4*j* | 0 | 0.2265(4) | 0.5 | 1 | 2.38(17) |
| O3 | 4*k* | 0 | 0 | 0.2142(3) | 1 | 1.16(18) |
| O4 | 4*l* | 0 | 0.5 | 0.2626(3) | 1 | 1.78(19) |
| O5 | 8*m* | 0.25 | 0.25 | 0.2363(3) | 1 | 1.84(10) |

The number in parentheses beside each entry indicates the estimated standard deviation referred to the last digit shown.

from *Pbnm* to *Ibmm* at $0.5<x<0.6$, *Ibmm* to *I*4/*mcm* at $x\approx0.7$, and *I*4/*mcm* to *Cmmm* at $0.8<x<0.9$. Evidently the lattice parameters of the basic perovskite subcell are nearly equal in the composition range $0.4\leqslant x\leqslant0.8$, similar to data reported by Vashook et al. [20]. Although there appears to be scatter in the reduced cell parameters, the volume of the basic subcell (the volume per formula unit) increases smoothly with composition, as shown in Fig. 3(b). The gradual increase of the basic cell volume with $x$ for $Ca_{(1-x)}La_{2x/3}TiO_3$ was first reported by Kim et al. [3] (although no structural solutions were provided by these authors), and it was attributed to the difference in ionic radii between $La^{3+}$ (1.36 Å) and $Ca^{2+}$ (1.34 Å), as well as the creation of cation vacancies.

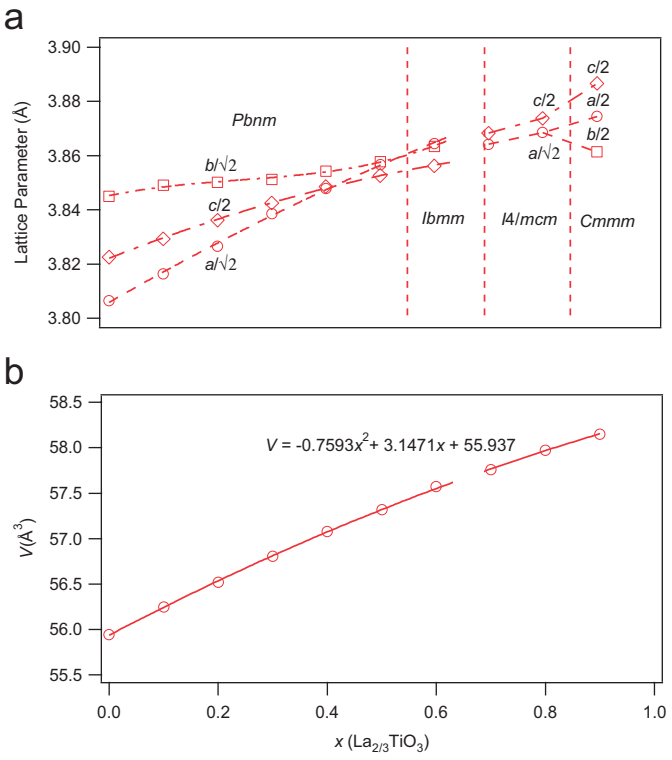


Fig. 3. Variation of (a) the reduced cell parameters, and (b) the basic subcell volume, with composition ($x$) for $Ca_{(1-x)}La_{2x/3}TiO_3$ at room temperature. The gap in the lines through the data points is intended to reflect the necessarily discontinuous nature of the transition from *Ibmm* to *I*4/*mcm*.

From the atomic co-ordinates we can estimate the angles of the out-of-phase ($\phi$) and in-phase ($\psi$) tilts of the $TiO_6$ octahedra, using the formulae listed in Table 2. It should be noted that in most structures (except *I*4/*mcm*) the out-of-phase tilt angle ($\phi$) can be estimated from the positions of either the apical or equatorial oxygen ions. The estimates obtained are very similar, as they should be (in the absence of shearing), and their average is presented in Fig. 4. As shown, the two tilt angles decrease progressively with the increase of La content. Note that the tilt angle for $x=0.7$ was essentially the same whether assuming the structure in *I*4/*mcm* or *Ibmm*.

### 3.2. Variable temperature studies

The purpose of the variable temperature studies was to determine, for each composition, the transition temperature marking the onset (or disappearance upon heating) of a particular octahedral tilting. Determination of the transition temperatures by diffraction methods depends on monitoring the corresponding superlattice reflections and in some instances the splitting/broadening of the main perovskite peaks, as summarised in Table 3. Among the listed transitions, there are two first-order transitions (*Pbnm* ↔ *I*4/*mcm* and *Ibmm* ↔ *I*4/*mcm*), and the rest are likely to be continuous transitions [10,13]. It should be noted that monitoring the main perovskite peaks for splitting/broadening is a less-reliable way to determine the

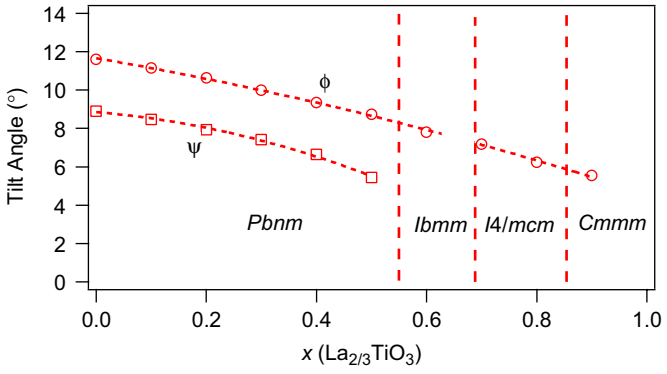


Fig. 4. Composition dependence of the octahedral tilting in $Ca_{(1-x)}La_{2x/3}TiO_3$ at room temperature.

Table 2
Formulae for tilt angle calculations [27,28,6]

| Structure, space group | Tilt axis | Out-of-phase tilt ($\phi$) | Tilt axis | In-phase tilt ($\psi$) |
|---|---|---|---|---|
| Orthorhombic *Pbnm* | $[110]_p$ | $\tan\phi\approx4\sqrt{2}z(O2)$<br>$\tan\phi\approx-2\sqrt{2}x(O1)$ | $[0\,0\,1]_p$ | $\tan\psi\approx2[y(O2)\text{-}x(O2)]$ |
| Orthorhombic *Ibmm* | $[110]_p$ | $\tan\phi\approx4\sqrt{2}z(O2)$<br>$\tan\phi\approx-2\sqrt{2}x(O1)$ | | No in-phase tilting |
| Tetragonal *I*4/*mcm* | $[001]_p$ | $\tan\phi=1\text{-}4x(O2)$ | | No in-phase tilting |
| Orthorhombic *Cmmm* | $[100]_p$ | $\tan\phi\approx2[z(O4)\text{-}z(O3)]$<br>$\tan\phi\approx2[y(O1)\text{-}y(O2)]$ | | No in-phase tilting |

Note that the lattice parameters have been removed from the formulae using $a\approx b\approx c/\sqrt{2}$ for *Pbnm* and *Ibmm*, and $a\approx b\approx c$ for *Cmmm*.

Table 3
List of phase transitions encountered in the $Ca_{(1-x)}La_{2x/3}TiO_3$ system, and associated changes in the diffraction patterns

| Phase transition | Main changes in diffraction patterns |
|---|---|
| *Pbnm* ($a^-a^-c^+$) → *I*4/*mcm* ($a^0a^0c^-$) | Disappearance of *M*-point reflections. |
| *First order* | Splitting/broadening of the $\{h00\}_p$ peaks into doublets with lower-intensity shoulders on the high-*d* side.[a] |
| *I*4/*mcm* ($a^0a^0c^-$) → *Pm*$\bar{3}$*m* ($a^0a^0a^0$) | Disappearance of *R*-point reflections. No more splitting/broadening of the $\{h00\}_p$ peaks. |
| *Continuous* | |
| *Pbnm* ($a^-a^-c^+$) → *Ibmm* ($a^-a^-c^0$) | Disappearance of *M*-point reflections. |
| *Continuous* | Splitting/broadening of the $\{h00\}_p$ peaks into doublets with lower-intensity shoulders on the low-*d* side. |
| *Ibmm* ($a^-a^-c^0$) → *I*4/*mcm* ($a^0a^0c^-$) | Intensities of the $\{h00\}_p$ doublet reversed, and the splitting roughly doubled [29,30]. |
| *First order* | |
| *Cmmm* ($a^-b^0c^0$) → *P*4/*mmm* ($a^0a^0c^0$) | Disappearance of *R*-point reflections. The $\{h00\}_p$ peaks change from triplets to doublets. |
| *Continuous* | |

[a] *Note*: the main $\{h00\}_p$ peaks are not required by symmetry to be a singlet in *Pbnm*, however it appears to be an "accidental" singlet for many $CaTiO_3$ related materials.

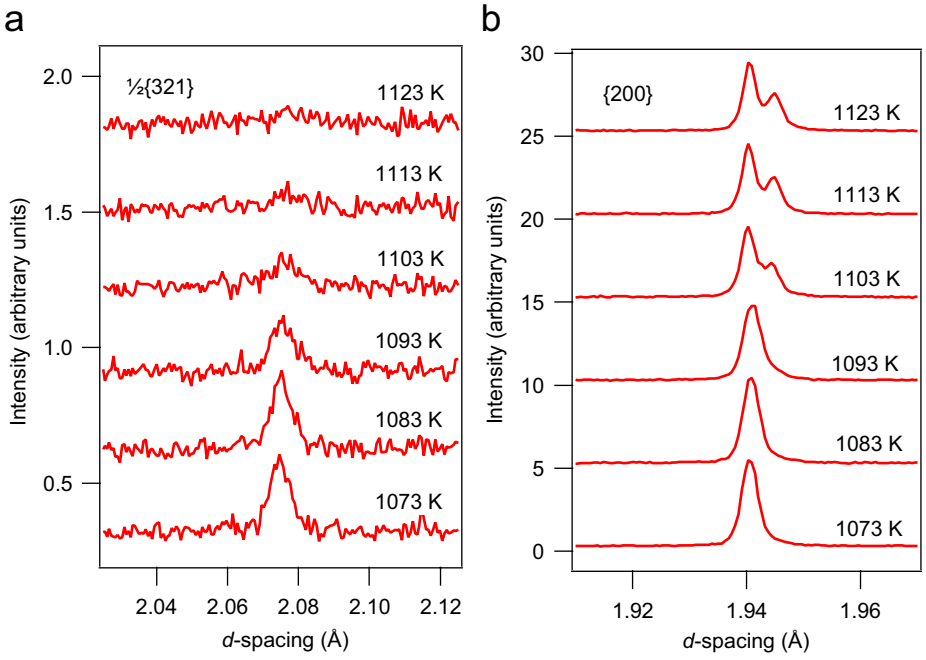


Fig. 5. Extracts from the neutron diffraction patterns for $Ca_{0.7}La_{0.2}TiO_3$ ($x = 0.3$)—as recorded in the back-scattering detector bank: (a) $2.025 < d < 2.125$ Å, and (b) $1.91 < d < 1.97$ Å, showing the evolution of the $\frac{1}{2}\{321\}_p$ and $\{200\}_p$ reflections (indexed on the basic perovskite subcell) as a function of temperature.

transition temperature for continuous phase transitions, as the splitting/broadening would disappear at a temperature below the actual transition due to limited instrument resolution.

Neutron (for $x = 0.3$) or synchrotron (for $x = 0.4$, 0.5, 0.7, 0.8 and 0.9) diffraction patterns were recorded from each sample at a number of temperatures, the temperature range being selected according to the transition temperature anticipated. Figs. 5(a) and (b) show extracts from neutron diffraction patterns for $Ca_{0.7}La_{0.2}TiO_3$ ($x = 0.3$), corresponding to the $\frac{1}{2}\{321\}_p$ (*M*-point) and $\{200\}_p$ reflections over the temperature range from 1073 to 1123 K. As seen, the intensity of the *M*-point reflection mostly disappeared at 1103 K (the residue intensity is likely due to the coexistence of both *Pbnm* and *I*4/*mcm* phases), and the main $\{200\}_p$ peak became a doublet at the same temperature. Therefore, we estimate the transition temperature from the *Pbnm* orthorhombic structure to the *I*4/*mcm* tetragonal one as roughly 1100 K for $Ca_{0.7}La_{0.2}TiO_3$ ($x = 0.3$). Similarly the transition temperature from *Pbnm* to *I*4/*mcm* is estimated, from X-ray synchrotron diffraction measurements, to be around 850 K for $Ca_{0.6}La_{0.27}TiO_3$ ($x = 0.4$).

Figs. 6(a) and (b) show the evolution of the $\frac{1}{2}\{310\}_p$ (*M*-point) and $\{400\}_p$ reflections in the temperature range of 450–700 K for $Ca_{0.5}La_{0.33}TiO_3$ ($x = 0.5$), as determined by synchrotron X-ray powder diffraction. While the intensity of the $\frac{1}{2}\{310\}_p$ reflection mostly disappeared at 550 K, the

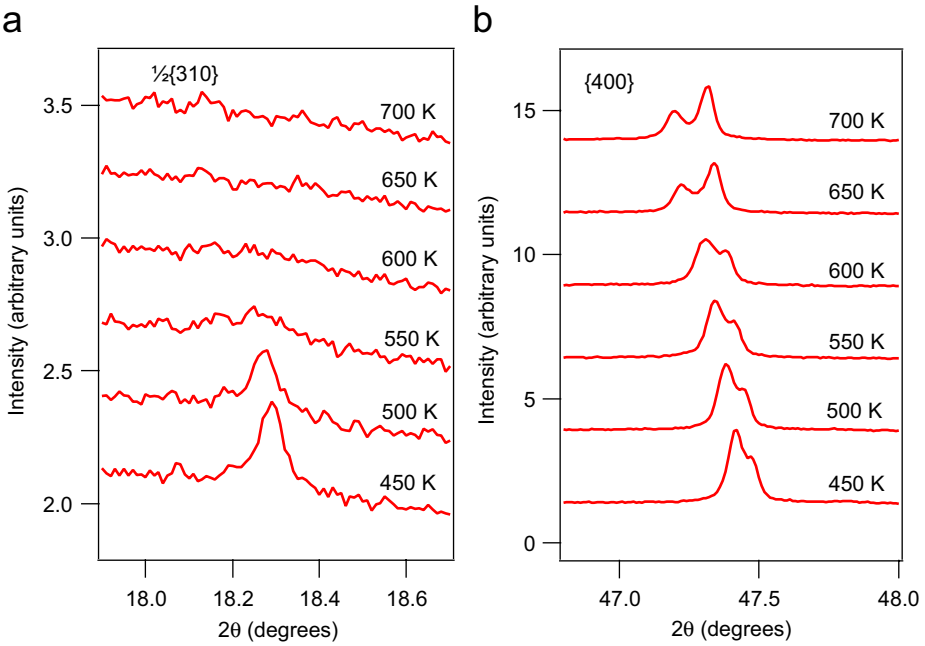


Fig. 6. Extracts from the synchrotron X-ray diffraction patterns for $Ca_{0.5}La_{0.33}TiO_3$ ($x = 0.5$) from 450 to 700 K: (a) $17.9 < 2\theta < 18.7^\circ$, and (b) $46.8 < 2\theta < 48.0^\circ$, showing the evolution of the $\frac{1}{2}\{310\}_p$ ($M$-point) and $\{400\}_p$ reflections (indexed on the basic perovskite subcell) as a function of temperature.

shape and splitting of the main $\{400\}_p$ peak did not show obvious change until 100 K later, suggesting the presence of two phase transitions: first from *Pbnm* to *Ibmm* at about 525 K then to *I*4/*mcm* at roughly 625 K. The intensity reversal of the $\{h00\}_p$ doublet and the (approximate) doubling of the peak splitting, when the orthorhombic *Ibmm* structure is transformed to the tetragonal *I*4/*mcm* structure, are demonstrated clearly in Fig. 6(b).

As described in the previous section, it is not possible to distinguish unambiguously between the structures in *Ibmm* and *I*4/*mcm* in the pseudo-cubic region at room temperature, based on powder diffraction data alone. We have encountered the same problem in the variable temperature studies. For $Ca_{0.3}La_{0.47}TiO_3$ ($x = 0.7$), synchrotron X-ray diffraction measurements were carried out from 100 to 350 K. The main difference in diffraction patterns within that temperature range is the slight narrowing of the main $\{h00\}_p$ peaks with increasing temperature (while the width of the $\{hhh\}_p$ peaks does not change). However, the $\{h00\}_p$ peaks show as a single (symmetric) peak even at 100 K, without any indication as to the structure being in *Ibmm* or *I*4/*mcm*. Similarly, for $Ca_{0.2}La_{0.53}TiO_3$ ($x = 0.8$), it is not possible to observe any splitting or asymmetric broadening of the main perovskite peaks in the pseudo-cubic temperature range of 300–750 K (the sharpening of the $\{h00\}_p$ peaks with increasing temperature was also observed). However, the determination of transition temperature to the cubic structure was straightforward, based on the disappearance of the *R*-point reflections, at around 775 K for $Ca_{0.2}La_{0.53}TiO_3$ ($x = 0.8$).

When $Ca_{0.1}La_{0.6}TiO_3$ ($x = 0.9$) undergoes its phase transition from the orthorhombic structure in *Cmmm* to the tetragonal structure in *P*4/*mmm*, the changes in the synchrotron X-ray diffraction patterns are much more obvious than for those samples in the pseudo-cubic range. The $\{h00\}_p$ peaks, being triplets in *Cmmm*, became doublets at 700 K, indicative of a tetragonal structure. The intensity of the *R*-point reflections vanished at the same temperature. Therefore, the transition temperature from *Cmmm* to *P*4/*mmm* is estimated as 675 K, which is about 100 K lower than that reported by Vasylechko et al. (784 K) [18]. Due to the large temperature interval used in their study (100 K), their transition temperature was obtained by linear extrapolation of the lattice parameters. Since the phase transition between *Cmmm* and *P*4/*mmm* may well be tricritical,[1] linear extrapolation could certainly overestimate the transition temperature. The other possible reason for the discrepancy is the thermometry difference between different instruments.

Fig. 7 incorporates all the transition temperatures derived from this study as well as those reported for $CaTiO_3$ ($x = 0$) and $Ca_{0.4}La_{0.4}TiO_3$ ($x = 0.6$). The published transition temperatures for the $CaTiO_3$ end member vary a great deal as reviewed recently by Ali and Yashima [15]. We have used the values reported by these authors: at 1498 K (*Pbnm* ↔ *I*4/*mcm*) and 1634 K (*I*4/*mcm* ↔ $Pm\bar{3}m$). For the $Ca_{0.4}La_{0.4}TiO_3$ ($x = 0.6$) sample, the published phase transition temperatures are around 450 K (*Ibmm* ↔ *I*4/*mcm*) and 1170 K (*I*4/*mcm* ↔ $Pm\bar{3}m$), respectively [19]. While the *Ibmm* ↔ *I*4/*mcm* phase transition is a

[1] Although we did not recognise tricritical character in our initial study of $La_{0.6}Sr_{0.1}TiO_3$ [6], a similar transition in $La_{1/3}NbO_3$ has been found to be of tricritical form [31].

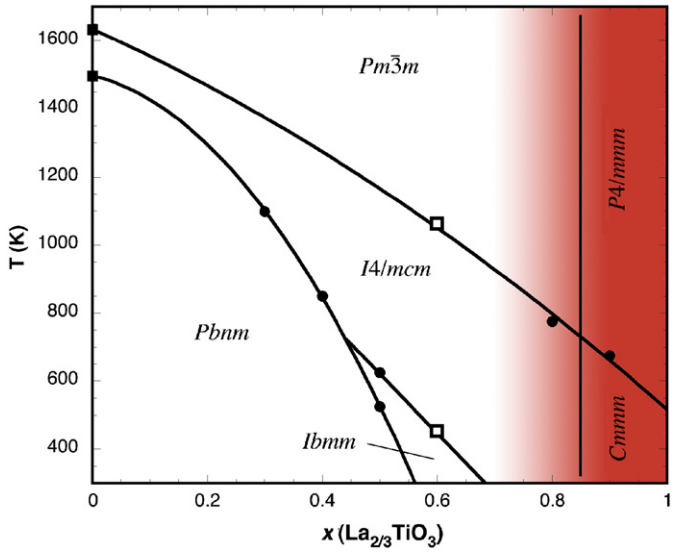


Fig. 7. Phase diagram for $Ca_{(1-x)}La_{3x/2}TiO_3$ based on transition temperatures obtained from in situ studies of samples with different compositions across the solid solution (solid dots are transition temperatures determined in this study, while the solid and open squares are previously published data [15,19]). The shading indicates the degree of cation/vacancy ordering: random to $x \approx 0.7$, then short range, and finally long range for $x \geqslant 0.9$.

(discontinuous) first-order one, the transition from $I4/mcm$ to $Pm\bar{3}m$ is expected to be tricritical.[2] Therefore, the $I4/mcm \leftrightarrow Pm\bar{3}m$ transition temperature of 1170 K would be overestimated by Vashook et al. [19] using linear extrapolation of the lattice parameters. In order to compare their transition temperatures with those derived from this study, we have shifted this transition temperature for $Ca_{0.4}La_{0.4}TiO_3$ by the same amount as the difference in the transition temperature for $Ca_{0.1}La_{0.6}TiO_3$ (see previous paragraph).

The data points marking the observed transition temperatures between $I4/mcm$ ($Cmmm$) and $Pm\bar{3}m$ ($P4/mmm$), corresponding to the transition from one out-of-phase octahedral tilt to no tilt, can be fitted reasonably well by a second-order polynomial function. The apparently smooth variation of this transition temperature with composition suggests that this transition, involving the removal of tilt, is little affected by the degree of cation/vacancy ordering. The phase boundary from $Pbnm$ to $I4/mcm$ (or $Ibmm$), corresponding to the disappearance of in-phase octahedral tilt, is also fitted by such a function. Since we only have two experimental data points along the $Ibmm \leftrightarrow I4/mcm$ phase boundary, linear extrapolation is used as a (very) rough estimation. The degree of cation/vacancy ordering, first random at low $x$, then short-range starting at $x \approx 0.7$, and finally long-range at $x \geqslant 0.9$, is indicated by shading in Fig. 7.

[2]As, for example, the analogous transition in $Ca_{0.3}Sr_{0.7}TiO_3$ [29].

## 4. Summary and conclusions

Compositions across the system $(1-x)CaTiO_3$–$xLa_{2/3}TiO_3$ have been studied using both neutron and synchrotron X-ray powder diffraction techniques, at various temperatures. The main conclusions have been incorporated into the schematic phase diagram in Fig. 7.

Structures in this system are characterised by octahedral tilting, as well as a layered cation/vacancy ordering on the perovskite $A$-sites. In-phase (+) and out-of-phase (−) octahedral tiltings are studied by monitoring the superlattice peaks, namely $M$-point (one integral and two half-integral indices, when indexed on the basic perovskite subcell), and $R$-point (all half-integral indices) reflections, respectively. Diffraction patterns were recorded at each composition as a function of temperature, in order to estimate the temperatures of disappearance (upon heating) or onset (upon cooling) of corresponding octahedral tilting. The cation/vacancy ordering is evidenced by the presence of peaks ($X$-point) with just one half-integral index. These peaks are sharp, indicative of long-range order for $x = 0.9$, and a significant tetragonal distortion is associated with this effect. The degree of cation/vacancy ordering decreases with $x$ (as evidence by much broader and significantly less intense $X$-point reflections), with the onset of short-range order at $x \approx 0.7$.

Based on high-temperature studies (Fig. 7), the room temperature structures are orthorhombic in $Pbnm$ for $0 \leqslant x \leqslant 0.5$ and in $Ibmm$ for $0.5 < x < 0.7$, then tetragonal in $I4/mcm$ for $0.7 \lesssim x < 0.9$, and finally orthorhombic in $Cmmm$ for $x \geqslant 0.9$. They are consistent with those determined from room temperature neutron diffraction patterns. It should be mentioned, however, that it is difficult to determine the structures for $x = 0.7$–$0.8$ based on diffraction data alone, as they were found to be metrically cubic to the resolution of our work. The assignment of space groups for these two samples (especially $x = 0.7$) at RT is therefore only tentative, as it relied upon the composition temperature phase diagram to a large extent. Based on the refinement results from the neutron diffraction patterns at room temperature, the perovskite subcell volume increases, while both the in-phase and out-of-phase octahedral tilt angles were found to decrease, with increasing $x$. Both these trends are consistent with the notion that the effective volume of two $La^{3+}$ ions plus a vacancy is greater than the volume of the three $Ca^{2+}$ ions they replace.

## Acknowledgments

We acknowledge the travel support to ISIS and Spring-8 for ZZ and CJH, provided by the Commonwealth of Australia under the Major National Research Facilities Program and the Australian Synchrotron Research Program, respectively. The neutron facilities at ISIS are operated by the Council for the Central Laboratory of the Research Councils (CCLRC), with a contribution from

the Australian Research Council (ARC). The synchrotron facilities at SPring-8 are supported by the Japan Synchrotron Radiation Research Institute (Proposal No. 2005A0355ND1a-np).

## References

[1] H. Yoshioka, S. Kikkawa, J. Mater. Chem. 8 (1998) 1821–1826.
[2] H. Yoshioka, J. Am. Ceram. Soc. 85 (2002) 1339–1341.
[3] I.-S. Kim, W.-H. Jung, Y. Inaguma, T. Nakamura, M. Itoh, Mater. Res. Bull. 30 (1995) 307–316.
[4] R.H. Mitchell, Perovskites–Modern and Ancient, Almaz Press, Thunder Bay, Ontario, 2002 Chapter 5.
[5] Y. Inaguma, T. Katsumata, M. Itoh, Y. Morii, J. Solid State Chem. 166 (2002) 67–72.
[6] C.J. Howard, Z. Zhang, J. Phys.: Condens. Matter 15 (2003) 4543–4553.
[7] M. Yashima, M. Mori, T. Kamiyama, K. Oikawa, A. Hoshikawa, S. Torii, K. Saitoh, K. Tsuda, Chem. Phys. Lett. 375 (2003) 240–246.
[8] C.J. Howard, G.R. Lumpkin, R.I. Smith, Z. Zhang, J. Solid State Chem. 177 (2004) 2726–2732.
[9] B.S. Thomas, N.A. Marks, P. Harrowell, Phys. Rev. B 74 (2006) 214109.
[10] C.J. Howard, H.T. Stokes, Acta Crystallogr. A 61 (2005) 93–111.
[11] A.M. Glazer, Acta Crystallogr. B 28 (1972) 3384–3392.
[12] A.M. Glazer, Acta Crystallogr. A 31 (1975) 756–762.
[13] Z. Zhang, C.J. Howard, K.S. Knight, G.R. Lumpkin, Acta Crystallogr. B 62 (2006) 60–67.
[14] H.F. Kay, P.C. Bailey, Acta Crystallogr. 10 (1957) 219–226.
[15] R. Ali, M. Yashima, J. Solid State Chem. 178 (2005) 2867–2872.
[16] M. Yashima, R. Ali, M. Tanaka, T. Mori, Chem. Phys. Lett. 363 (2002) 129–133.
[17] R. Ali, M. Yashima, M. Tanaka, H. Yoshioka, T. Mori, S. Sasaki, J. Solid State Chem. 164 (2002) 51–59.
[18] L. Vasylechko, V. Vashook, U. Guth, in: N. Sammes, A. Smirnova, O. Vasylyev (Eds.), Fuel Cell Technologies: State and Perspectives, Springer, Dordrecht, The Netherlands, 2005, pp. 373–380.
[19] V. Vashook, L. Vasylechko, M. Knapp, H. Ullmann, U. Guth, J. Alloys Compd. 354 (2003) 13–23.
[20] V. Vashook, L. Vasylechko, N. Trofimenko, M. Kuznecov, P. Otchik, J. Zosel, U. Guth, J. Alloys Compd. 419 (2006) 271–280.
[21] R.M. Ibberson, W.I.F. David, K.S. Knight, Rutherford Appleton Laboratory Report RAL92-031, 1992.
[22] E. Nishibori, M. Takata, K. Kato, M. Sakata, Y. Kubota, S. Aoyagi, Y. Kuroiwa, M. Yamakata, N. Ikeda, Nucl. Instrum. Methods A 467–468 (2001) 1045–1048.
[23] H.M. Rietveld, J. Appl. Crystallogr. 2 (1969) 65–71.
[24] A.C. Larson, R.B. von Dreele, General Structure Analysis System (GSAS), Los Alamos National Laboratory Report LAUR 86-748, 2000.
[25] B.H. Toby, J. Appl. Crystallogr. 34 (2001) 210–213.
[26] D.I. Woodward, I.M. Reaney, Acta Crystallogr. B 61 (2005) 387–399.
[27] B.J. Kennedy, C.J. Howard, B.C. Chakoumakos, J. Phys.: Condens. Matter 11 (1999) 1479–1488.
[28] M.A. Carpenter, C.J. Howard, B.J. Kennedy, K.S. Knight, Phys. Rev. B 72 (2005) 024118.
[29] C.J. Howard, R.L. Withers, Z. Zhang, K. Osaka, K. Kato, M. Takata, J. Phys.: Condens. Matter 17 (2005) L459–L465.
[30] M.A. Carpenter, C.J. Howard, K.S. Knight, Z. Zhang, J. Phys.: Condens. Matter 18 (2006) 10725–10749.
[31] B.J. Kennedy, C.J. Howard, Y. Kubota, K. Kato, J. Solid State Chem. 177 (2004) 4552–4556.